Naval Research Laboratory

DTIC FILE COPY

AD-A197 965

Hanex Simulations of Laser-Target Interactions:
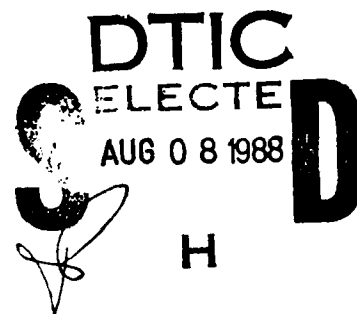# I. Radiation Processes

JOHN L. GIULIANI, JR AND MARGARET MULBRANDON

Plasma Physics Division

ELLIS HYMAN

Science Applications International Corporation
McLean, VA 22101

DTIC
ELECTE
AUG 0 8 1988
D
H

June 8, 1988

REPORT DOCUMENTATION PAGE

Form Approved
OMB No 0704-0188

1a REPORT SECURITY CLASSIFICATION	1b RESTRICTIVE MARKINGS
UNCLASSIFIED	

2a SECURITY CLASSIFICATION AUTHORITY	3 DISTRIBUTION / AVAILABILITY OF REPORT
	Approved for public release; distribution
2b DECLASSIFICATION / DOWNGRADING SCHEDULE	unlimited.

4 PERFORMING ORGANIZATION REPORT NUMBER(S)	5 MONITORING ORGANIZATION REPORT NUMBER(S)
NRL Memorandum Report 6223	

6a NAME OF PERFORMING ORGANIZATION	6b OFFICE SYMBOL (If applicable)	7a NAME OF MONITORING ORGANIZATION
Naval Research Laboratory	Code 4780	

6c. ADDRESS (City, State, and ZIP Code)	7b ADDRESS (City, State and ZIP Code)
Washington, DC 20375-5000	

8a. NAME OF FUNDING / SPONSORING ORGANIZATION	8b OFFICE SYMBOL (If applicable)	9 PROCUREMENT INSTRUMENT IDENTIFICATION NUMBER
Defense Nuclear Agency	RAAE	

8c. ADDRESS (City, State, and ZIP Code)	10 SOURCE OF FUNDING NUMBERS			
Washington, DC 20305	PROGRAM ELEMENT NO	PROJECT NO	TASK NO	WORK UNIT ACCESSION NO
		RB RC		

11 TITLE (Include Security Classification)

Hanex Simulations of Laser-Target Interactions: I. Radiation Processes

12. PERSONAL AUTHOR(S)
Giuliani, J.L., Jr., Mulbrandon, M. and Hyman, Ellis*

13a TYPE OF REPORT	13b TIME COVERED		14 DATE OF REPORT (Year Month Day)	15 PAGE COUNT
Interim	FROM _____	TO _____	1988 June 8	37

16 SUPPLEMENTARY NOTATION
(See page ii)

17	COSATI CODES		18 SUBJECT TERMS (Continue on reverse if necessary and identify by block number)
FIELD	GROUP	SUB-GROUP	Laser plasmas, Photo-chemistry,
			Blast waves, Radiation

19 ABSTRACT (Continue on reverse if necessary and identify by block number)

Numerical simulations of the laser-target interaction and subsequent plasma blowoff expansion for the PHAROS III experiment are presented using the HANEX code. This report emphasize the properties of the radiation field and the photo-absorption physics in the background gas. The multi-frequency radiation transport technique employed in HANEX is fully described. Likewise, the phenomenological treatment in HANEX for the ionization, dissociation, and heating in the background gas resulting from radiation deposition is presented. The evolution of the background plasma due to radiation deposition is studied from the time of the peak of the laser pulse to 60 nsec later. Model spectra of the heated plasma blowoff predict strong emission lines from highly ionized nitrogen and aluminum in the cavity.

20 DISTRIBUTION / AVAILABILITY OF ABSTRACT	21 ABSTRACT SECURITY CLASSIFICATION
☒ UNCLASSIFIED/UNLIMITED ☐ SAME AS RPT ☐ DTIC USERS	UNCLASSIFIED

22a NAME OF RESPONSIBLE INDIVIDUAL	22b TELEPHONE (Include Area Code)	22c OFFICE SYMBOL
J.D. Huba	(202) 767-3030	Code 4780

DD Form 1473, JUN 86   Previous editions are obsolete

S/N 0102-LF-014-6603

16. SUPPLEMENTARY NOTATION

This work was sponsored by DNA under "RB RC/Atomspheric Effects and Mitigation," Work Unit Code and Title: RB RC/00166, Plasma Structure Evolution.

*Science Applications International Corporation, McLean, VA 22101

CONTENTS

QUALITY
INSPECTED
2

Accession For

NTIS   GRA&I   ☑
DTIC TAB   ☐
Unannounced   ☐
Justification_____

By_____
Distribution/

Availability Codes

Dist	Avail and/or Special
A-1	

iii

HANEX SIMULATIONS OF LASER-TARGET INTERACTIONS:
I. RADIATION PROCESSES

I. INTRODUCTION

Over the past several years the Plasma Physics Division at the Naval Research Laboratory has run a laser-target experiment with the objectives of modeling physical processes occuring in a high altitude nuclear explosion (HANE) [1]. This latter program is under the auspices of the Division of Atmospheric Effects at the Defense Nuclear Agency. In this regard the experiment is intended to provide a physical understanding of nuclear disturbed environments in order to provide reliable predictions of the degradation of radar, communications and, potentially, advanced weapons systems.

The experiment, which has been recently upgraded and is referred to as PHAROS III, illuminates one side of a planar target with a beam from a neodymium laser. The target, usually comprised of aluminum, is a few microns thick and the laser energy is typically 100 Joules. The laser intensity at the target surface is about 10^{13} Watts/cm^2 and the laser wavelength is 1 micron. During the laser pulse of ~ 5 nanoseconds FWHM, the front side of the target absorbs the laser light predominantly by inverse bremsstrahlung and heats up to a temperature of ~ 1 keV. The resulting overpressure leads to a forward ablative blowoff with velocities of ~ 10^7 cm/sec toward the laser, and a slower backward acceleration of the rearside of the target. When a background gas, typically molecular nitrogen, is present in the surrounding chamber at pressures ranging from 0.5 to 5 Torr, the forward expanding debris forms a blast wave as it sweeps up the background. The blast wave reaches 1 cm at ~ 100 nanoseconds. The rearward moving debris also forms a shock wave in the nitrogen, but its precise character depends on the target thickness. This pressure regime is suitable for studying strong to moderate collisional coupling between the debris and background gas. At lower pressures, a kilogauss magnetic field can be produced around the target in order to study collisionless coupling mechanisms.

As part of the theoretical effort to understand the blast wave formation in the high pressure regime, a numerical simulation code was developed within the Plasma Physics Division[2]. This simulation code modeled the dynamics with a Lagrangian difference scheme in one spatial dimension. It began with a

laser pulse impinging on a cold, aluminum, planar target. The target disassembly occurred by heating due to inverse bremsstrahlung absorption of the laser beam. While the target remained in the near solid phase, the ideal equation of state was corrected to include the zero temperature isotherm of solid aluminum. The subsequent vaporization and hydrodynamic expansion of the debris and swept-up background gas was followed out to ~ 1 cm assuming perfect coupling, i.e., a contact discontinuity was maintained between the debris and background. The nearly radial expansion of the debris-air interface was accounted for by employing a unique oblate spheroidal geometry with the symmetry axis along the initial laser beam. The initial target position is in the central part of the geometry which is planar. Separate ion and electron temperatures were included as well as the thermal conduction from each species. Magnetic fields were not included for these high pressure models. In order to follow the atomic physics starting from the dense, solid phase to the low density gas phase, a time-dependent chemistry model was used developed including all the ion and neutral species of both aluminum and nitrogen. Saha ionization equilibrium conditions are maintained while the aluminum is near solid density. After vaporization, both the debris and background chemistry evolved in a non-equilibrium manner. A simple radiation transport scheme was developed to model the heating of the backside of the target due to x-rays from the critical surface at the front side.

Some of the conclusions of the numerical simulations were concerned with the nature of the cavity or bubble which forms behind the forward moving blast wave. It was found that this region is hotter (T_e ~ 60eV) and more rarefied (n_e ~ $2 \times 10^{17} cm^{-3}$) than the surrounding blast wave (T_e ~ 20eV and n_e ~ $3 \times 10^{18} cm^{-3}$). However, the cavity is highly overionized for its temperature, with the debris species predominantly Al^{+9}, Al^{+10}, and Al^{+11}. The results for the blast wave region are in good agreement with the experimental results [3], as is also the electron density in the cavity, at least for that part of the cavity near the blast wave [4]. The high charge state result in the cavity was unexpected, though no experimental determination one way or the other is presently known. There are several simplifications in the above described numerical code which might weaken the conclusions. First, the assumption of a contact discontinuity between the debris and air is not strictly valid, even at 5 Torr pressure. The aluminum

and nitrogen will mix to some degree and subsequent charge exchange between the two elements could lower the charge state of aluminum in the mixing region. Second, the simplified radiation treatment used only 12 frequency bins, did not specifically account for resonant line emission, and the chemistry model did not include self-absorption within each grid cell. The neglect of these radiative effects could alter the cavity temperature.

In order to improve the previous calculations and solidify the conclusions we have upgraded the simulation code in two major ways. The new code is referred to as the HANEX code. For the first upgrade, the cross-streaming of the aluminum debris through the nitrogen background is followed approximately. Since the basic simulation code is hydrodynamic, it models the ion and electron gases as a Maxwellian distribution with small deviations due to temperature gradients. By allowing for additional deviations to the distribution function due to composition and partial pressure gradients, relative drift velocities between the aluminum ions, nitrogen ions, and electrons arise. The model is consistent as long as the relative drift velocities are small compared to the sound speed. The resulting mixing by diffusion of the highly charged aluminum and the low charged nitrogen in the cavity region leads to charge exchange between the two species. The theory behind our drift calculation and charge exchange cross-sections will be reported on in a companion report.

The second major upgrade to the original code deals with radiation transport. We have increased the frequency resolution of the radiation spectrum from 12 to 166 frequency bins. This permits resolving the edges of the ground states of all aluminum and nitrogen species and including 41 resonance transitions. We have also improved the calculation of the emission and absorption processes. The theory behind our second upgrade, along with a discussion of the background air chemistry, will be discussed in §II of this report. The processes of radiation absorption, subsequent ionization, and heating in the background plasma are addressed in §III. We present details of these processes at a position 2 cm away from the target and over the time between the peak of the laser pulse to just before the shock front sweeps over this position. Also model spectra from the simulation runs will be presented in §III. These spectra are calculated as if a spectroscopic camera viewed the experiment perpendicular to the laser axis. The highly ionized

emission lines from resonant transitions which appear in the model spectra are indicative of the highly ionized cavity. Direct comparison with observed spectra in the UV to X-ray energy bandpass should provide one direct test of the validity of our simulation models.

II. RADIATION AND PHOTO-CHEMISTRY

A. Emission, Absorption, and Transport.

The treatment of radiation in the HANEX code follows the same basic transport scheme used in the earlier simulation code; the radiation intensity is calculated along a single ray according to the fundamental radiative transfer equation,

$$\frac{d\ I_\nu}{d\ s} = -\kappa_\nu I_\nu + j_\nu \,. \tag{1}$$

Here I_ν is the radiation intensity in ergs/cm^2·sec·sd·Hz, κ_ν is the absorption coefficient in cm^{-1}, and j_ν is the emission coefficient in ergs/cm^3·sec·sd·Hz. Each of these quantities are carried at position s and frequency ν, where s is the path length along the single ray parallel to the laser axis and passing through the target center.

In the earlier code the intensity, absorption, and emission coefficients were averaged over 12 frequency bins. In the HANEX code, however, the resolution of the radiation spectrum is vastly improved by employing 166 frequencies between 1 eV and 10 keV. The radiation transport is then calculated frequency-by-frequency and the absorbed radiation energy is averaged into frequency bins. The frequencies are chosen to resolve a number of spectral features composed of edges and lines. Each ground state of aluminum and nitrogen leads to an absorption edge for the outermost valence electron subshell, giving 20 edges. Each edge is resolved by two frequencies, one slightly above and the other slightly below the edge.

Furthermore, 41 strong resonance lines between the ground and excited states are included, with at least one from each ionic species. The specific lines are listed by ion species and energy in Table I. (The letters in parentheses refer to Fig. 7 discussed in section III.b.) Each resonance line is resolved by three frequencies, one at line center and the other two in the line wings. The line resolution is too crude for determining line profiles for it treats each line as a triangular distribution, but the resolution is sufficient to account for the energy exchange between the dynamics and radiation.

The plasma emission processes include free-free bremsstrahlung, free-bound radiative recombination, and bound-bound emission lines. The absorption processes include free-free, bound-free, bound-bound, and inner shell. For the free-free processes the absorption coefficient is

$$\kappa_{\nu,ff} = \sigma_{\nu,ff} n_e = \frac{4}{3}\left(\frac{2\pi}{3}\right)^{1/2} \frac{e^6}{m_e^{3/2} c (kT_e)^{1/2}} g_{ff} n_e n_i \langle Z^2 \rangle \frac{\left(1-e^{-h\nu/kT_e}\right)}{h\nu^3}. \quad (2)$$

where e is the elementary charge, m_e is the electron mass, c is the speed of light, k is the Boltzmann constant, T_e is the electron temperature, n_e is the electron density, n_i is the ion density, and $\langle Z^2 \rangle$ is the averaged squared-charge, i.e.,

$$\langle Z^2 \rangle = \sum_j \frac{n_j Z_j^2}{n_i}$$

and n_j is the number density of ions in ionization stage j with charge Z_j. From Kirchoff's law the corresponding emission coefficient is

$$j_{\nu,ff} = \frac{8}{3}\left(\frac{2\pi}{3}\right)^{1/2} \frac{e^6}{m_e^{3/2} c^3 (kT_e)^{1/2}} g_{ff} n_e n_i \langle Z^2 \rangle e^{-h\nu/kT_e}. \quad (3)$$

The free-free Gaunt factor g_{ff} was fixed at unity throughout the range 1 eV < $h\nu$ < 10 keV.

For the bound-free processes, let $\sigma_{\nu,bf}(j,k)$ be the cross-section for photo-absorption from ionization stage j and excited level k to the next higher ionization stage j+1. Using the Milne relation to connect the cross-section for photo-absorption to the cross-section for induced recombination

from ion stage j+1 to excited level k of ion j, the photo-absorption cross-section, corrected for induced recombination, is found to be

$$\sigma'_{\nu,bf}(j,k) = \sigma_{\nu,bf}(j,k)\left(1 - \Theta e^{-h\nu/kT_e}\right), \tag{4}$$

where

$$\Theta = \frac{n_{j+1}n_e}{n_{j,k}}\frac{U_j}{U_{j+1}}\frac{g_{j,k}}{g_j}\left(\frac{m_e}{2\pi kT_e}\right)^{3/2}\frac{h^3}{m_e^3}e^{I_{j,k}/kT_e}. \tag{5}$$

Here $I_{j,k}$ is the ionization energy of excited level k of ionic state j, the statistical weight of the same level is $g_{j,k}$, and U_j is the partition function for the ionic state j. The corresponding emission coefficient due to recombination to level k of ion state j is given by

$$j_{\nu,bf}(j,k) = n_{j,k}\,\sigma_\nu(j,k)\frac{2h\nu^3}{c^2}\Theta\,e^{-h\nu/kT_e}. \tag{6}$$

Several approximations have been employed in these equations in the HANEX code. First, only ground states are considered in the bound-free processes. Second, every photo-absorption cross-section, σ_ν, is assumed to fall off as $1/\nu^3$ above the threshold frequency. Finally, the combination of the partition functions and statistical weights in Θ is taken as unity, as it would be in local thermodynamic equilibrium (LTE). The cross-section, $\sigma_{\nu,bf}$, at threshold is the maximum of two values: (i) one based on the radiative recombination coefficient from the Milne relation (see Appendix 1 of Ref. 5), and (ii) the other based on the inner shell opacity data discussed in the next paragraph. The first value insures detailed balance in regions of high density.

In addition to the valence shell absorption process discussed above we included the inner shell opacity. This process is important in the backside of the target and in the ambient background gas where the flux of high energy photons formed at the frontside of the laser-heated target is absorbed. The

dependence of the absorption cross-section on energy is taken from Ref.6 for the neutral species. For the ionized atoms the same energy dependence is used but the threshold frequency for each of the shells shifts to higher energies. These shifts are given by Roothaan-Hartree-Fock calculations of the atomic level binding energies in Ref.7.

For bound-bound photo-absorption from the ground level of ion stage j to excited state k, the cross-section corrected for stimulated emission, is

$$\sigma_{\nu,bb}(j\to k) = \frac{\pi e^2}{m_e c} f_{jk} \phi_\nu \left(1 - \frac{n_{j,k} g_{j,k}}{n_j g_j}\right) , \tag{7}$$

where f_{jk} is the oscillator strength for the transition and ϕ_ν is the line profile function. Under conditions of LTE for the excited states the term in parentheses reduces to $1-\exp(-h\nu_{jk}/kT)$. The corresponding line emission coefficient is

$$j_{\nu,bb}(j\to k) = n_{j,k} A_{kj} \frac{h\nu_{jk}}{4\pi} \phi_\nu , \tag{8}$$

with the relation between the Einstein coefficients being

$$\frac{\pi e^2}{m_e c} f_{jk} = \frac{B_{jk} h\nu_{jk}}{c} ; \qquad g_j B_{jk} = g_k B_{kj}; \qquad B_{kj} = \frac{c^3}{8\pi h\nu_{jk}^3} A_{kj} . \tag{9}$$

Resolution of the line profile would require many frequencies over the Doppler line profile $\phi_{\nu,D}$. We have simplified the analysis by adopting a triangular line profile which vanishes at $\nu_{jk}-\Delta\nu$ and $\nu_{jk}+\Delta\nu$, where $\Delta\nu$ is the full width at half maximum of a Doppler profile. At line center the profile function is then $\phi_\nu(jk) = 1/\Delta\nu$, which specifies the cross-section for the line absorption in eqn.(7).

The cross talk between our time-dependent chemistry and radiation transport proceeds in the following manner. After a hydro timestep δt the chemistry integrator is called. The chemistry package advances the species' abundances over δt and simultaneously calculates for each grid cell, h, the

frequency and time integrated emission from bremsstrahlung, recombination, and line radiation. To complete the solution for the timestep δt in our time-splitting scheme, the radiation package is called last. It begins by redistributing the integrated emission (from the chemistry package) into a frequency grid for each cell according to the frequency dependence of the different j_ν's in eqns. (3), (6), and (8). Likewise the absorption coefficients are evaluated from eqns. (2), (4), and (7) at each frequency, and the optical depth through each cell h, of width Δ_h, is formed as $\tau_{\nu,h+1/2} = n\sigma_\nu\Delta_h$. The transport equation (1) is now solved for the radiation energy E_ν at the cell interfaces, once in the forward direction (+)

$$E^+_{\nu,h+1} = E^+_{\nu,h} e^{-\tau_{\nu,h+1/2}} + \frac{1}{2} j_{\nu,h+1/2} 4\pi \, Vol_{h+1/2} \delta t \delta \nu \frac{(1 - e^{-\tau_{\nu,h+1/2}})}{\tau_{\nu,h+1/2}} ,$$

and once in the rearward direction (-),

$$E^-_{\nu,h} = E^-_{\nu,h+1} e^{-\tau_{\nu,h+1/2}} + \frac{1}{2} j_{\nu,h+1/2} 4\pi \, Vol_{h+1/2} \delta t \delta \nu \frac{(1 - e^{-\tau_{\nu,h+1/2}})}{\tau_{\nu,h+1/2}} ,$$

where $j_{\nu,h+1/2}$ is the total radiation emitted at frequency ν from all processes, δt is the time step, $\delta \nu$ is the frequency interval around the frequency ν, and $Vol_{h+1/2}$ is the volume of cell h+1/2. The factor 1/2 in front of $j_{\nu,h+1/2}$ means that one half of the photons move forward and the other half backward. The boundary conditions at the outermost cell interfaces are that no radiation energy enters the system. The radiation energy absorbed in cell h at frequency ν is given by

$$H_{\nu,h+1/2} = (E^+_{\nu,h} + E^-_{\nu,h+1}) e^{-\tau_{\nu,h+1/2}}$$

$$+ j_{\nu,h+1/2} 4\pi \, Vol_{h+1/2} \delta t \delta \nu \left[1 - \frac{(1 - e^{-\tau_{\nu,h+1/2}})}{\tau_{\nu,h+1/2}} \right]$$

8

The last term in this equation is the amount of energy that is both emitted and then re-absorbed within cell h. The chemistry package also determines this quantity, but under slightly different conditions. If one subtracts from $H_{\nu,h+1/2}$ the amount of radiated energy, ΔH, which the chemistry routine already re-absorbed within cell h, the remainder gives the heating of the electrons in cell h; $H'_{\nu,h+1/2} = H_{\nu,h+1/2} - \Delta H_{\nu,h+1/2}$. The amount of radiation lost from the system is given by the sum of E^+ at the forward cell interface and E^- at the rearward cell interface. If molecular nitrogen is present in a cell, $H_{\nu,h+1/2}$ is modified as discussed below.

Before returning to the next hydro and chemistry step the radiation routine calculates an escape probability for each frequency from

$$P_{\nu,esc} = \frac{1 - e^{-\tau_{\nu,h+1/2}}}{\tau_{\nu,h+1/2}}$$

The chemistry routine then uses this probability in the next timestep to determine the fraction of emitted radiation by a given process which is re-absorbed within the same cell ($\propto \Delta H$). This feature takes account of the re-absorption of radiated energy in optically thick cells and therefore effectively decreases the radiative emission leaving a cell.

The scheme we have just described has been tested for consistency by analyzing a high density 10eV material. The resulting spectrum reproduced the blackbody limit to within a percent. Furthermore, the simulation runs conserved total radiative, chemical, internal and kinetic energy to within 3%.

The above scheme does have the limitation that it cannot handle photo-pumping and photo-ionization from one cell to another. An energy-consistent simulation of this process in a time-dependent, non-equilibrium chemistry, which is coupled to the radiation transport, would require major code development and testing. At present those photons which would lead to pumpimg or ionization are treated the same as the remaining photons. i.e., they are deposited as electron heating. This approximation of converting all the absorped non-local photons to pure electron heating is reasonable in regions near local thermodynamic equilibrium (LTE). However, in the cold, neutral background the photo-ionization due to the non-local photons

predominantly determines the state of the gas. The special treatment of radiation deposition for this region is discussed next.
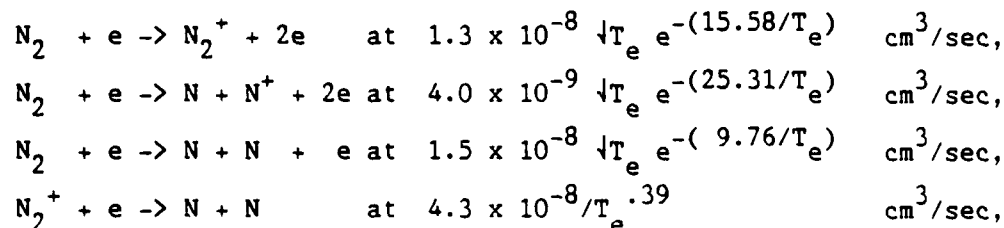

B. Photo-Chemistry of the Background Gas

The phenomenology in the region ahead of the shock is complex and far from LTE. In this section we describe the essential approximations adopted to model the chemistry for this region in the HANEX code. During the laser pulse the ionization and heating of the background gas is driven by the absorption of the UV and X-rays from the laser heated target. In this deposition phase the electron temperature in the background gas is not well defined , i.e., the electron distribution is not Maxwellian. An absorbed high energy photon will ionize or dissociatively ionize background N_2 molecules and create energetic electrons. These electrons will lose most of their energy by further ionization and/or electronic excitation of molecules and atoms. Thermal equilibration of the fresh, high energy electrons with the older, lower energy electron population takes place primarily through collisional de-excitation of these excited states. Radiation losses are negligible. Further, some portion of the electron energy will excite vibrational levels of the N_2 molecules. But the relaxation time for vibrational energy is long, about 10^{-6} sec for a 5 Torr background pressure, so vibrational temperature is not well defined either. The neutrals and ions will be heated through collisional quenching of the vibrationally excited states. Following the time dependent development of these processes in detail is beyond the scope of this work. In order to approximate the state of the background we have developed a simplified model to account for these ionization, dissociation and heating processes.

The absorbed photon energy is apportioned according to the following prescription. First, the cross section for N_2 is assumed to be twice that of N. Then, for every 35 eV of the absorbed photon energy one ion is created, either N^+ or N_2^+, depending on the relative abundance of N and N_2. In addition, in the case of absorption by N_2 molecules, for every 55 ev of absorbed photon energy one N_2 is dissociated. The remaining energy after ionization or dissociation of N_2 is divided evenly between the heavy

particles and the electrons. For photo-ionization by N all the remaining energy is given to the electrons. Apportioning some of the energy to the heavy particles compensates approximately for the energy fed in from vibrational states, which is not tracked in detail.

Time dependent chemistry for atomic nitrogen of all charge states has been described in a previous report[2]. In order to follow the behavior of the background gas, N_2 chemistry is also required. The following two-body reactions and rate coefficients have been added to the chemistry model;

$$N_2 + e \rightarrow N_2^+ + 2e \quad \text{at} \quad 1.3 \times 10^{-8} \sqrt{T_e}\, e^{-(15.58/T_e)} \quad cm^3/sec,$$

$$N_2 + e \rightarrow N + N^+ + 2e \quad \text{at} \quad 4.0 \times 10^{-9} \sqrt{T_e}\, e^{-(25.31/T_e)} \quad cm^3/sec,$$

$$N_2 + e \rightarrow N + N + e \quad \text{at} \quad 1.5 \times 10^{-8} \sqrt{T_e}\, e^{-(9.76/T_e)} \quad cm^3/sec,$$

$$N_2^+ + e \rightarrow N + N \quad \text{at} \quad 4.3 \times 10^{-8}/T_e^{.39} \quad cm^3/sec,$$

where T_e is the electron temperature in eV for an equivalent Maxwellian distribution. In the last reaction the products are really N and $N(^2D)$. However, the $N(^2D)$ is assumed to be immediately deexcited by electron collisions with the 2.38 eV/reaction distributed to the electron gas.

Although this prescription may seem in some degree arbitrary, it can be justified by the results of a much more detailed calculation performed by two of the authors using a similar spectrum for the deposited radiation[8]. The results of this simple model for fractional ionization and dissociation, as well as the temperatures, are in qualitative agreement with the detailed code.

III. DISCUSSION OF RESULTS

We begin by noting that the total radiation loss from the laser-target interaction is not large. Figure 1a displays the temporal energy budget for our standard run, vis., a 100 J laser energy shot on a 5.6 um thick aluminum target with 1.5 Torr background pressure of N_2. Of the total laser energy, half is assumed to be focused and absorbed into a spot o. 125 um radius on the target. For a laser pulse of 10 nsec this results in a peak intensity of

~1.6x10^{13} Watts/cm^2. (Note that the 125 μm is the radius of the neck in the oblate spheriodal geometry of the HANEX code pictured in Fig.1 of Reference 2.) Figure 1a in the present report shows that the time-integrated energy lost through radiation is ~20% of the absorbed laser energy. However, radiation does play a significant role in transfering energy from hotter regions to colder ones. Initially the laser radiation is absorbed by inverse bremsstrahlung in a thin surface layer of the target. Secondary radiation from this hot, dense region competes with electron thermal conduction and the impulse shock wave in transfering energy to the rear side of the target. Forward propagating radiation from this same hot region is the main source of energy deposition in the background gas during the laser pulse. At later times, radiation from the frontside blast wave becomes important both for determining the condition of the background and the energy loss from the system. Figure 1b displays the positions of the frontside, as well as the rearside, shockfronts as a function of time. In the next subsection we will focus our attention on the properties of the background gas and blast wave. In addition to energy transfer, radiation losses can be used as a diagnostic tool. In the following subsection we will discuss how UV and X-ray spectra of the blowoff plasma may be used to discern the charge species in the cavity region within the blast wave.

A. Radiation Deposition in the Background Gas.

The deposition of energy in the gas at early times depends on the spectrum of the radiation from the target. This ,however, depends on the plasma conditions in the target. In Fig. 2 are plots of the electron and ion density, velocity, average ion charge, and electron and ion temperatures vs. radius at a time near the peak of the laser pulse (5.48 nsec after the pulse begins). The left boundary in the plots coincides with the rear edge of the foil and the extent on the right side includes only part of the blowoff region. Three distinct regions can be enumerated in these plots. A cold dense backside with some rearward expansion near the foil edge, a low density, hot blowoff, and a transition region with steep gradients in temperature, density, and charge state. The blowoff region is composed of high charge states of Al and will emit radiation mostly from K-shell lines

and recombination. Because the density is relatively low, especially toward the front, most of the generated radiation escapes in the forward direction. From the backside through the transition layer the Al charge states increase, from +3 to +10. The radiation produced in these regions will therefore be from L-shell lines, recombination and bremsstrahlung. Because of the high densities in these two regions, the line radiation is very optically thick and almost none escapes. Even the recombination edges have a optical depth greater than one, so much of the spectral structure will be absorbed. The radiation which does emerge resembles a blackbody at a temperature near that of the front of the high density region. This radiation will pass through the blowoff region unattenuated because it lies below the K-absorption edge. Thus the radiation from the target at the peak of the laser pulse looks like a blackbody near 40 eV plus a high energy component of Al K-shell edges and lines.

A plot of the radiation intensity at a position 2 cm from the target along the laser axis, for the case described above, is presented in Fig. 3a. Superimposed on the target spectrum, one can clearly see the absorption edge due to the intervening N and N_2 between the target and the above position. The energy absorbed by the background at this 2 cm location as a function of the photon energy is shown in Fig. 3b. The spectral regions that are most important for absorption at this time of the peak laser pulse lie between 40 and 200 eV due to the L-edge of nitrogen. Another absorption peak at 450 eV is due to the nitrogen K-edge. The radiation from 15 to 40 eV, which actually has the maximum absorption crossection, has already been absorbed by atoms nearer the target. The electrons produced by photo-ionization at 2 cm will therefore be quite energetic.

After the peak of the laser pulse the plasma rapidly expands and the emitted radiation per unit volume drops. However, the amount of radiation that reaches 2 cm declines more slowly. Although the emitting target material is optically thick during the laser pulse, it has a small surface area. After the material expands it becomes optically thinner and the volume emissivity specifies the radiation. The large volume of the expanded plasma maintains the amount of radiation energy incident at 2 cm. As the blowoff region expands into the nitrogen background, line radiation from the blast wave becomes an important source of energy deposition in the more distant

background.   In Figs. 4a and 4b the   incident and absorbed spectrum,
respectively, are shown at a time 60 nsec after the peak of the laser pulse.
At this time both spectra are dominated by line radiation from the blast wave
as is evidenced by the series of sharp lines near 30 - 60 eV. The fraction
of the total energy incident at 2 cm in each of four spectral intervals is
plotted as a function of time in Fig. 5a. The shift from energetic photons
at early times to less energetic ones at late time can be seen in this
figure. In Fig. 5b the fraction of the total energy absorbed at 2 cm is
shown for the same intervals.   The most energetic interval contains photons
above 667 eV. This radiation is from the K-shell of aluminum and originates
in the blowoff region.   The   radiation originating mostly from the backside
region is divided into two spectral intervals,   153 eV to 398 eV, and 398 eV
to 667 eV.   The lowest interval, photon energy less than 153 eV, is
predominately from the cold target regions at early times and from line
radiation from the blast wave at later times.

The effect of the deposition of the radiation on the background gas
depends on the energy absorbed per atom. In Fig. 6a the time integrated and
the rate of energy absorbed per atom at 2 cm is shown. The nearly constant
rate of energy absorption after 20 nsec is due to the fact that the decrease
in the radiative output from the shock front per unit area is compensated by
a decrease in the distance to the shock as it moves outward and closer to 2
cm. The densities of N_2, N, N_2^+, N^+ and the electrons n_e are presented vs.
time in Fig. 6b. We note that the fraction of ionization is only a few
percent during the laser plulse but rises to nearly 15% just before the time
that the shock overruns the position at 2 cm.

B. Model Spectra of the Blowoff Plasma.

Inclusion of the physics of radiation emission and absorption in a
simulation code is important for modeling the dynamical evolution of the
laser-target interaction and blowoff.   In addition, a numerical method for
radiation transport can create model spectra which can be compared with
experiment. It often happens that spectroscopic observations provide the
most detailed data of a plasma experiment.

To produce model spectra we have employed the previously described radiation transport scheme with several modifications in a postproccesser. The first modification is a change in the transport direction. In the hydro-chemistry-radiation code the radiation was transported along a ray parallel to the laser beam axis. This approach successfully accounts for the transfer of radiation energy from an inner plasma region to an outer one. In the laser experiment all spectroscopic observations are performed with the camera line-of-sight perpendicular to the laser axis. To compare with these observations the postprocessor solved the radiation transport equation (1) along a set of rays perpendicular to the laser axis. Each ray, along which the transport equation is to be solved, begins at the far side of the plasma emitting region. After passing across the laser axis and through the near side of the emitting plasma, the ray encounters an extended region (10 cm long) of neutral N_2. The addition of this absorbing region surrounding the blowoff plasma is the second modification. Transport through it models the fact that between a spectroscopic camera and the experiment lies an extended region of nitrogen at the background pressure. Finally, we assume in the postprocessor that the plasma blowoff is spherical about the laser target. This modification from the geometry of the hydrodynamic code, which is oblate spheroidal, permits a great simplification in computing the intensity along line-of-sight rays which pass above or below the laser axis. Viewing the blowoff plasma perpendicular to the laser axis, the emergent intensity along all rays which pass at a distance r from the target is equal to the solution of the transport equation for the ray which crosses the laser axis at position r. Geometrical considerations then allow the calculation of an approximate model spectra at any spatial position.

As an example, we study the spectra arising from a laser produced plasma for a 5 Torr background pressure and 20 J laser energy on a 4.6 micron thick aluminum target of radius 125 microns. Artificial masks were used so that only the forward moving blowoff plasma would contribute to the model spectra. Specifically, if the target and blowoff plasma are enclosed by a large circle, the back side of the circle away from the laser beam was blocked off. Further, a disc of radius 0.25 cm was centered on the initial position of the target to block out emission from the dense target material. To maximize the emission intensity, the model spectra was time integrated over the first 100

15

nsec of the run. Figure 7a shows the resulting model spectrum. The low energy continuum is due to bremsstrahlung and the high energy jagged continuum results from recombination edges of nitrogen and aluminum. The large gap in the continuum between 15 eV and ~50 eV is due to the inner shell absorption by the 10 cm long path of extended nitrogen. The strong emission lines are labeled by letters according to Table I. The model spectrum includes emission from the blast wave formed in the background nitrogen gas as well as emission from the cavity within the blast wave. This cavity is composed of aluminum and nitrogen. The latter has been mixed in by diffusic The high energy lines, particularly those above ~100 eV, are emitted from the cavity. The parent ionic species of these lines from both aluminum and nitrogen reveal a highly charged region. The lower energy lines arise from the blast front. In the simulation for this run the electron temperature is ~20 eV in the blast wave, but rises to ~70 eV in the cavity. Hence, as has been noted in the Introduction, the cavity is overionized for its temperature. This situation is a remnant of the early-time freezing out of the charge state; the initially hot target material cools by expansion at a faster rate than the recombination rate. Early in time the blast wave was also much hotter and the swept-up nitrogen was thereby ionized up. Due to the difficulties in directly measuring the density and temperature of the frontside cavity region, we suggest that experimental spectra in the UV and X-ray domain should be quite revealing in light of the predicted spectra of Fig. 7a. For comparison, a similar model spectra of the rear side is presented in Fig. 7b. In this case the masks were turned over to block out the frontside and target emission. At late times the cavity stretches from the frontside blastwave, through the initial target position, and backwards to near the rearward moving shock. Hence some of the moderately high ionization stages appear both in the front and backside spectra; for instance, lines i,j,m,n,q,r,t,and u. Other lines from moderately high ionization stages of aluminum, such as h,k,o,and p, appear on the backside but not the frontside spectrum. The striking difference between the backside and frontside spectra is the strong lines from low ionization stages of aluminum (lines a and b) on the rearside spectrum only, in contrast with the cluster of lines (v-z) from Al^{+11} and Al^{+12} on the frontside spectrum only. These features from the spectra reflect the details of the simulation run:

16

the frontside cavity is more highly ionized than the rearside one, while the rearward moving blast wave is denser and cooler than its frontside counterpart.

IV. SUMMARY AND DISCUSSION

In this report we have presented a review of the multi-frequency radiation transport scheme used in the NRL HANEX simulation code. Likewise we have discussed the model incorporated in HANEX for the absorption, ionization, excitation, and heating of the background nitrogen resulting from the deposition of the high energy target and blast wave radiation. Results were presented for the evolution of the background nitrogen from the time of the peak in the laser pulse to 60 nsec later. Model spectra of the cavity and blast wave region indicate strong lines from highly ionized aluminum and nitrogen. This result suggests that UV and X-ray spectroscopy of the plasma blowoff could be used to investigate the nature of the cavity and verify our long-standing prediction of a hot (50-70 eV), overionized ($<Z> \sim 5$-10) cavity within the blast wave.

The transport scheme and deposition model described in section II employed several simplifying assumptions. First, the boundaries of the oblate spheroidal geometry, so useful for the dynamic expansion, impose the artificial condition that the radiation is constrained to diverge through a cone of 45 degrees half-angle. At late times when the radiation is predominately from the blast wave this condition will produce a small error since any deposition occurs nearby. But at early times this condition will over estimate the flux at a distant background position. Fortunately, the time integrated radiation escaping the target at early times is low compared to the final value of about 15 to 20%. Second, the treatment of line transport is very approximate and leads to an overestimate of the line absorption when the lines are moderately thick as in the dense target regions; no allowance is made for line radiation to escape through broad wings of the line profile. Third, the assumption that all the energy absorbed in a cell is put into heating of the electrons will not cause errors if the cell is near equilibrium, as in the dense target region and the blast

17

wave. However, when the target material falls to low density (the cavity) the plasma is far from equilibrium. This material does not absorb much energy because the absorption cross-section is near zero for the low energy photons that dominate our spectrum. In this region a more careful treatment of absorbed radiation would somewhat decrease the electron temperature. The problem of depositing radiation in the cold neutral background gas has only been approximated. The energy absorbed in the nitrogen K-shell will lead to further, though lower energy, radiation and therefore not be deposited locally. This process could effect the temperatures of neutrals and ions, as well as the electrons. It is believed that the prescription used for the deposition process should provide values for densities to within a factor of two.

ACKNOWLEDGEMENT

REFERENCES

1. B. H. Ripin, A. W. Ali, H. R. Griem, J. Grun, S. T. Kacenjar, C. K. Manka, E. A. McLean, A. N. Mostovych, S. P. Obenschain, and J. A. Stamper, in Laser Interaction and Related Plasma Phenomena, Vol. 7, p. 857, ed. by H. Hora and G. Miley, Plenum (1986).

2. J. L. Giuliani, Jr. and M. Mulbrandon, "Numerical Simulation of the Laser-Target Interaction and Blast Wave Formation in the DNA/NRL Laser Experiment," NRL Memorandum Report 5762 (1986).

3. J. Stamper, B. H. Ripin, E. A. McLean, C. K. Manka, and A. N. Mostovych, reported at the "Early-Time High Altitude Working Group Meeting", held at NRL, November 1984.

4. J. Stamper, reported at the "Early-Time High Altitude Working Group Meeting", held at NRL, May 1985.

5. D. E. Osterbrock, Astrophysics of Gaseous Nebulae, (W. H. Freeman and Company: San Francisco), 1974.

6. F. Biggs and R. Lighthill, "Analytic Approximations for X-Ray Cross Sections II," Sandia Laboratories Report SC-RR-71 0507 (1971).

7. E. Clementi and C. Roetti, "Roothaan-Hartree-Fock Atomic Wavefunctions," Atomic Data and Nuclear Data Tables, 14, 177 (1974).

8. M. Mulbrandon and E. Hyman, 1983, unpublished.

TABLE I

TRANSITION ENERGY (in eV) OF TRANSPORTED RESONANCE LINES

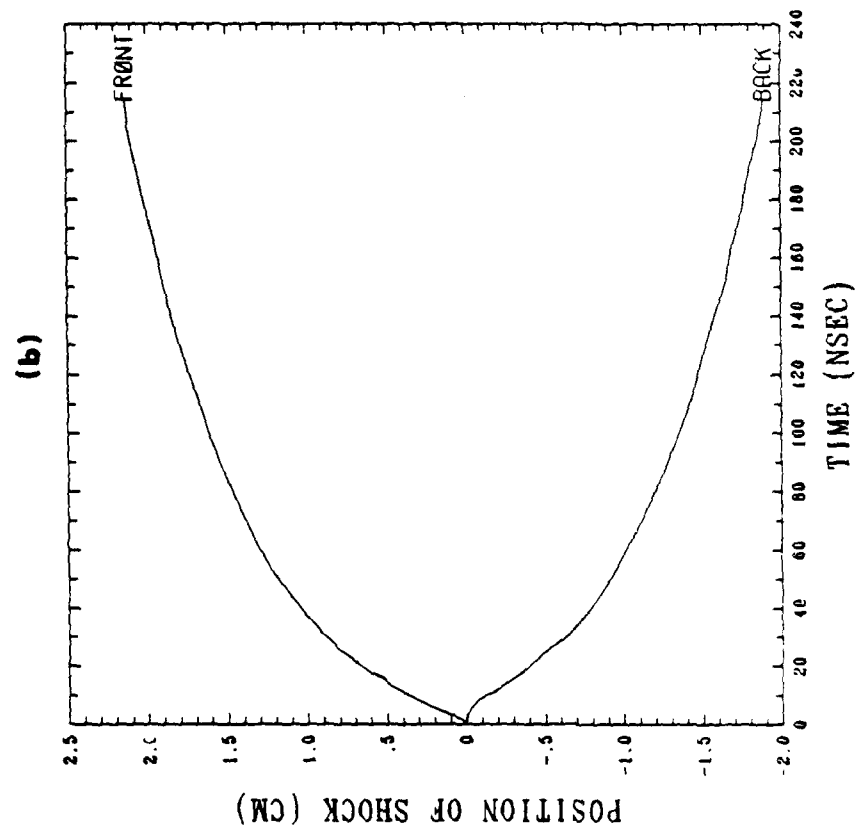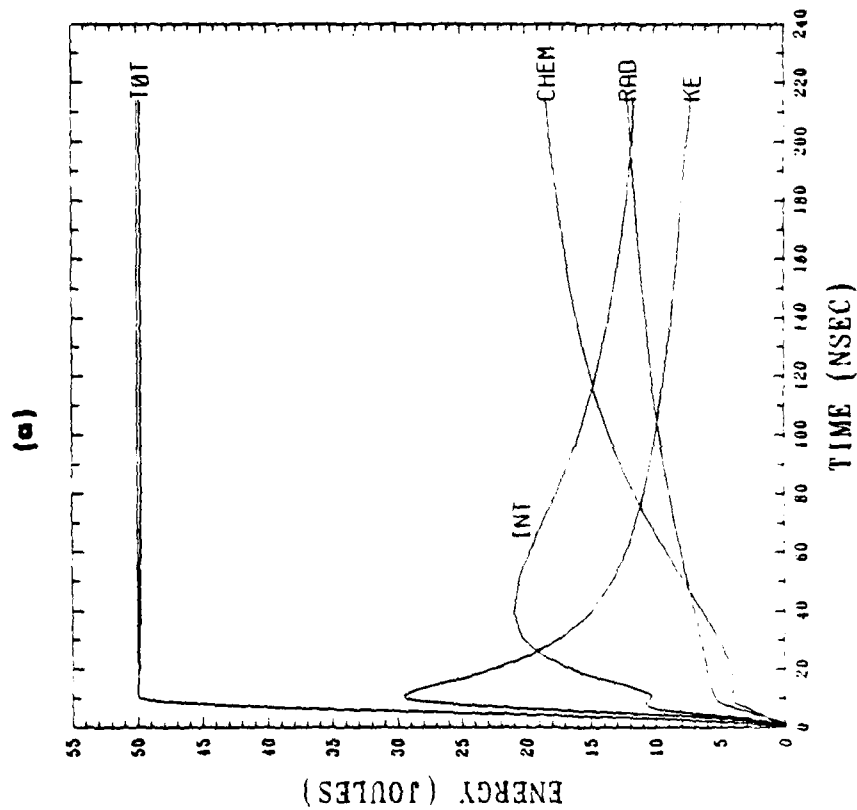|				
Al I	4.01	5.23	5.78	
Al II	7.42(b)			
Al III	6.67(a)	17.81		
Al IV	77.44(o)	94.95(p)		
Al V	44.34(k)			
Al VI	40.03(h)			
Al VII	34.92			
Al VIII	37.95	49.74(l)		
Al IX	43.73(j)	31.8	41.0(i)	
Al X	37.24(g)	238.5(q)		
Al XI	22.30	256.6(r)		
Al XII	1598.0(v)	1869.0(x)	1964.0(y)	
Al XIII	1724.0(w)	2042.0(z)		
N I	10.33			
N II	11.43(d)	13.53(f)	19.22	23.22
N III	12.51(e)	16.23	18.08	33.12
N IV	16.20	50.15(m)		
N V	10.00(c)	59.24(n)		
N VI	430.67(s)	497.94(t)		
N VII	500.0(u)			

Fig. 1(a)-Energy budget in time for the standard run described in the text.
CHEM is the instantaneous energy locked up in ionization potential. RAD
is the time-integrated amount of energy lost from the system through
radiation. INT is the instantaneous thermal energy of random motion,
and KE is the instantaneous kinetic energy of directed motion.
1(b)-The positions of the forward moving (FRONT) and rearward moving
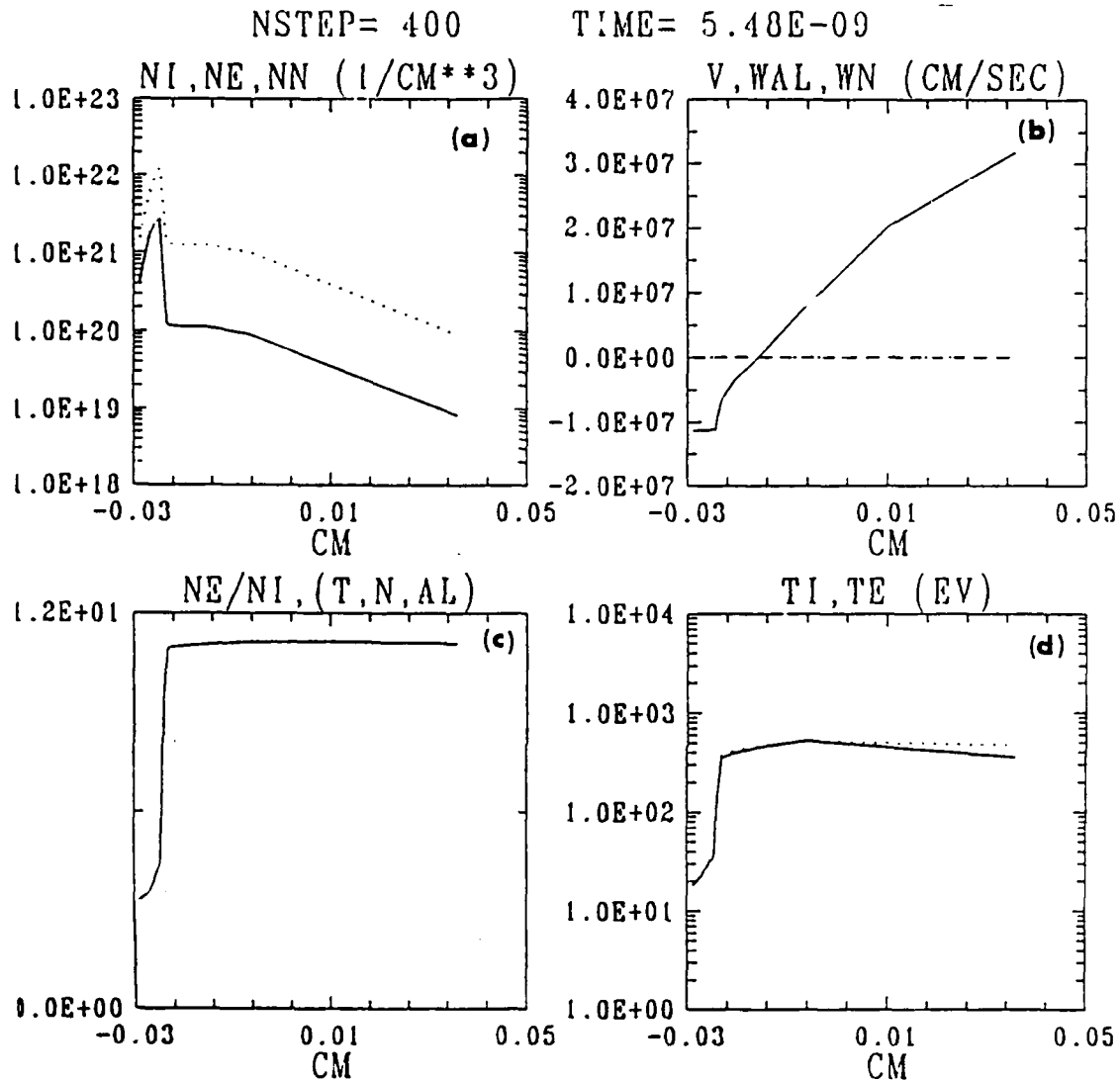(BACK) shock fronts as a function of time.

21

Fig. 2. Structure of the target and blowoff region at the peak of the laser pulse for the standard run. 2(a)-The ion (solid), electron (dotted), and neutral (dashed) number densities. 2(b)-The mean velocity. The drift velocities WAL and WN are negligible over this region. 2(c)-The mean charge state. 2(d)-The ion (solid) and electron (dotted) temperatures.

22

(b)

PHOTON ENERGY (EV)

SPECTRAL ABSORPTION(Watts/ev cm³)

(a)

PHOTON ENERGY (EV)
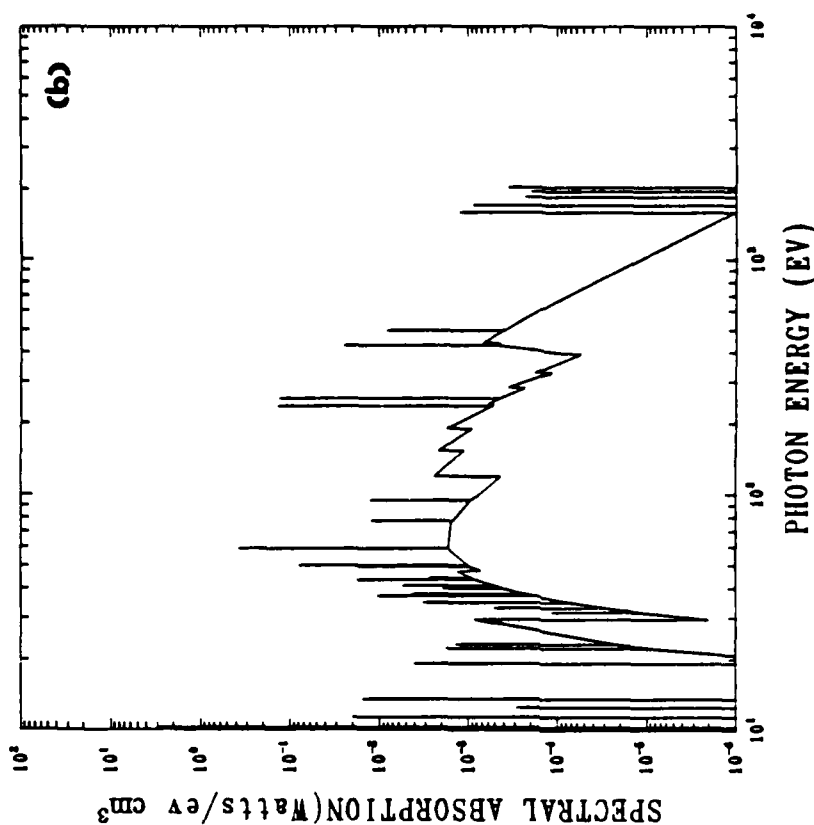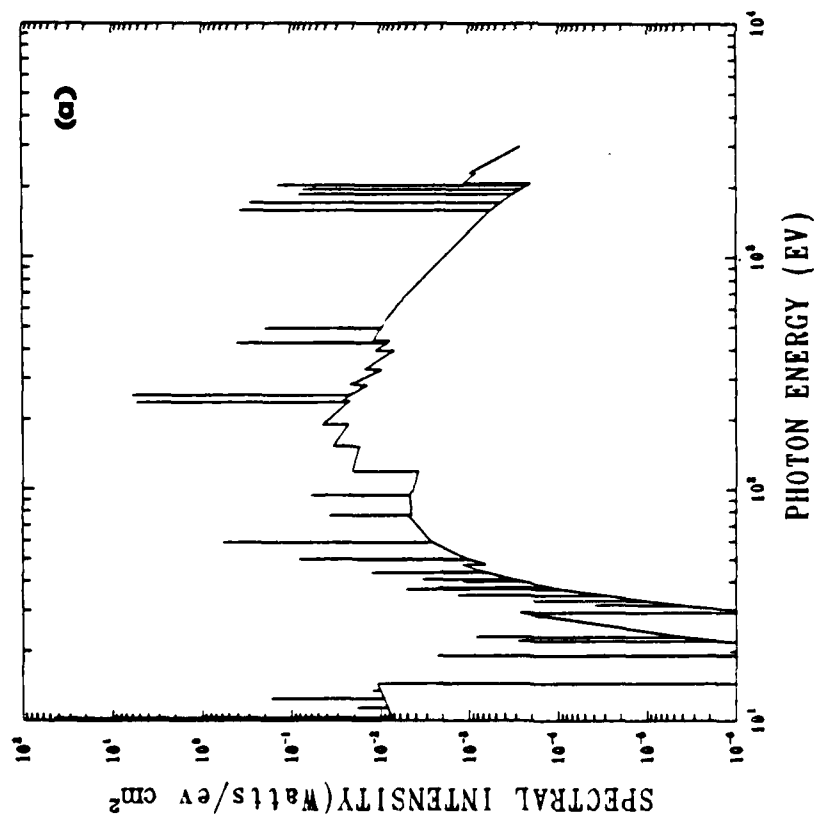
SPECTRAL INTENSITY(Watts/ev cm²)

Fig. 3(a)-Spectrum of the incident radiation intensity from the heated target at the peak of the laser pulse as a function of photon energy for a position 2 cm from the target and along the laser axis. 3(b)-Spectral distribution of the absorbed energy for the same conditions. The initial conditions are again for the standard run.
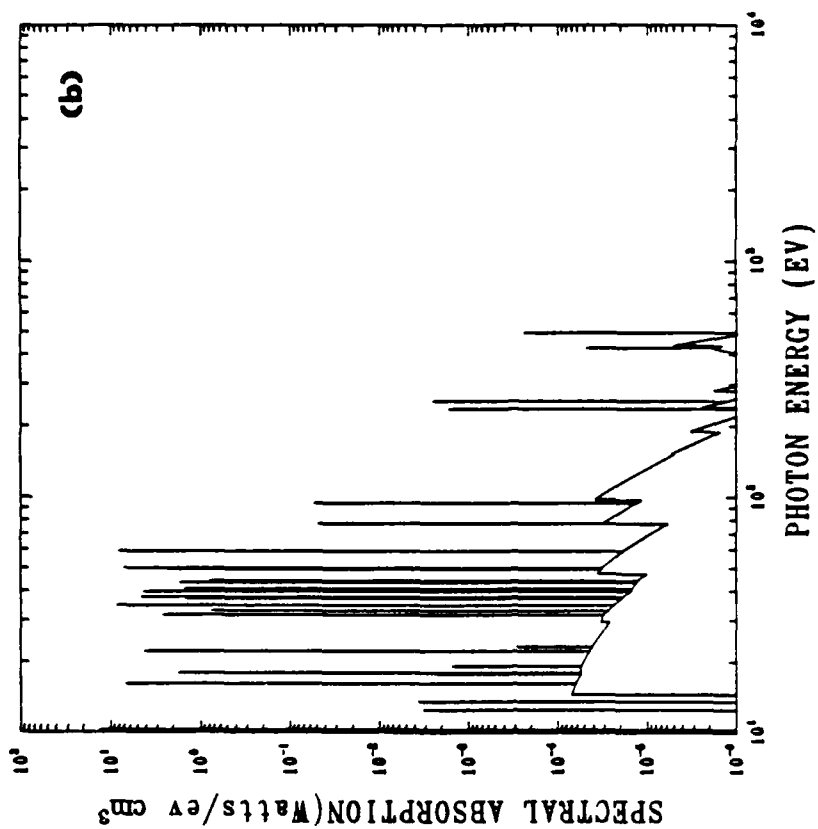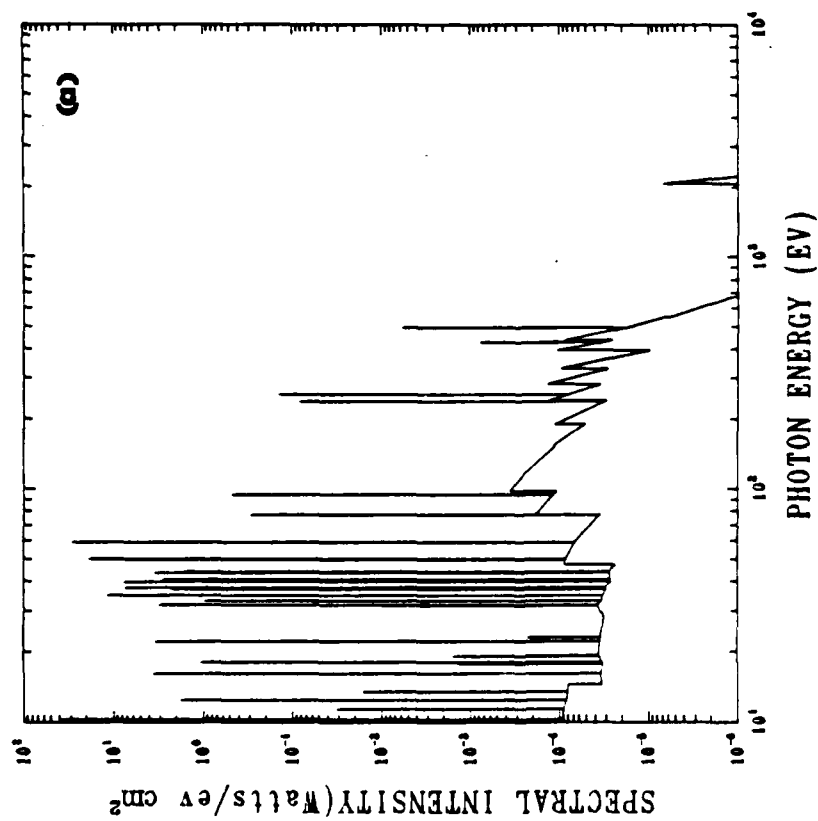
23

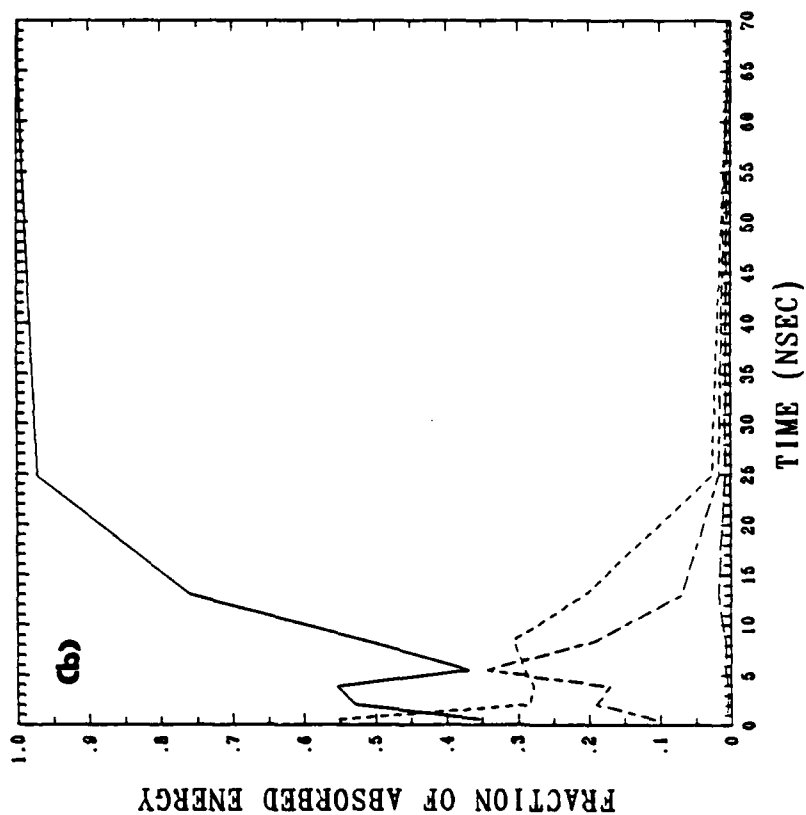Fig. 4(a) and 4(b)-Same as Figures 3(a) and 3(b) except at 60 nanoseconds after the peak of the laser pulse.

24
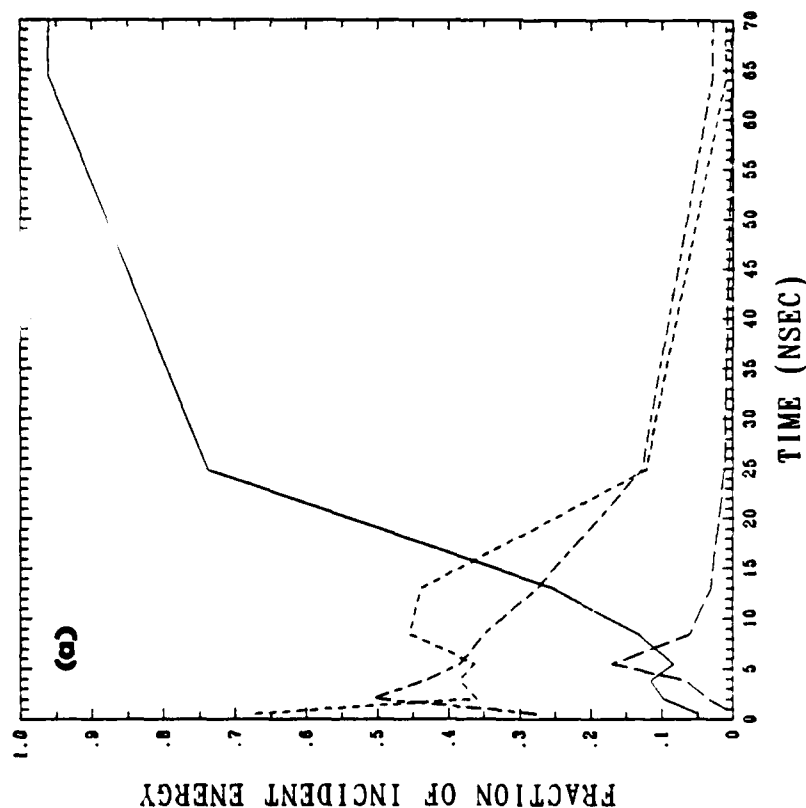
Fig. 5(a)-The fraction of incident energy in four bands seen at 2 cm from the target as a function of time; solid for E < 153 eV, dash-dash-dot for 153 < E < 398 eV, short dash for 398 < E < 667 eV, long dash for E > 667 eV. 5(b)-Same as Figure 5a except for the fraction of absorbed energy. The initial conditions are again for the standard run described in the text.
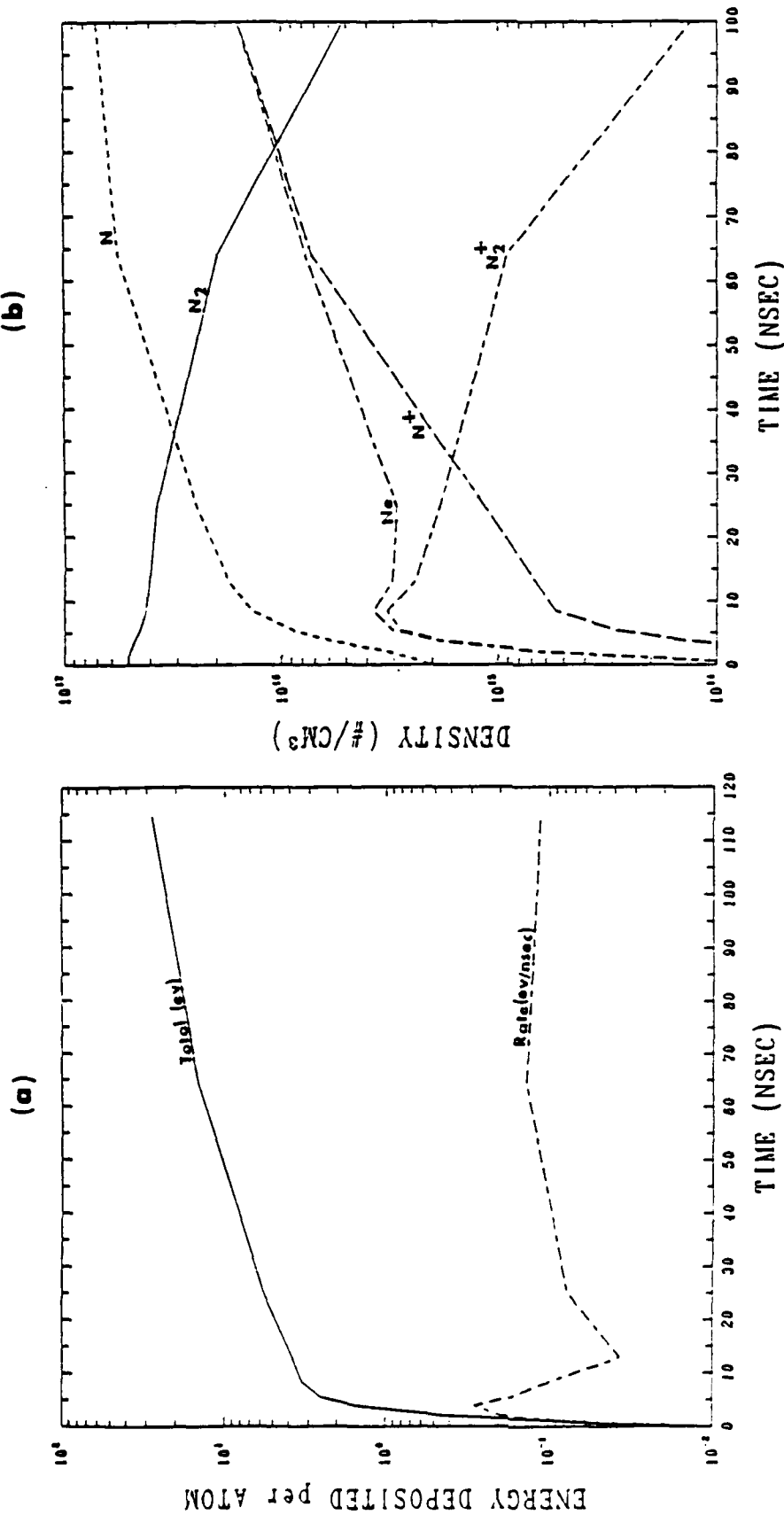
25

Fig. 6(a)–The time integrated and differential energy absorbed per atom in the background gas at 2 cm from the target as a function of time. 6(b)–The density of different species in the background gas at 2 cm as a function of time. The initial conditions are agian for the standard run described in the text.
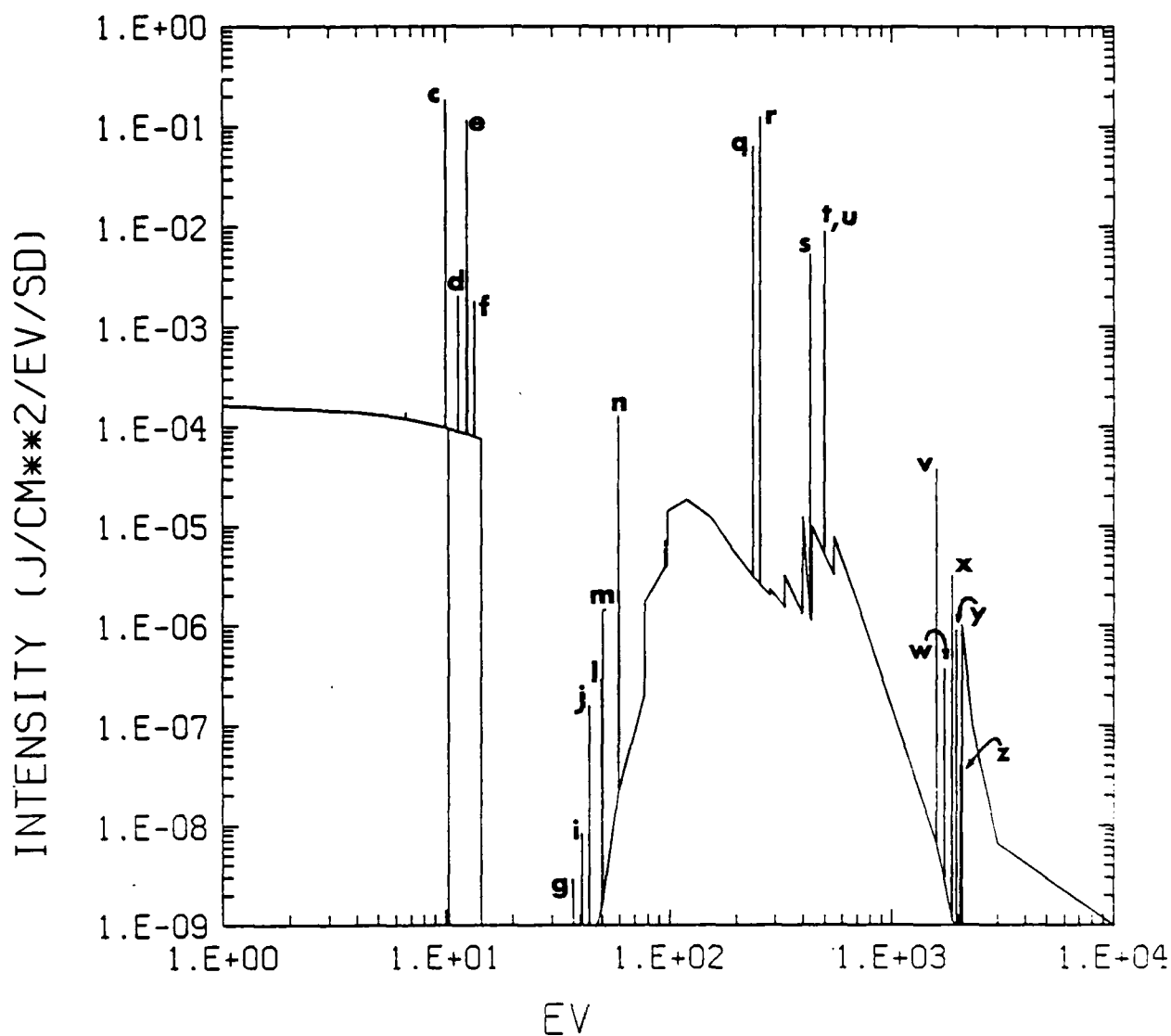
Fig. 7(a)-A synthetic spectrum of the forward moving plasma blowoff and blast wave integrated in time (up to 100 nsec) and in space. The rearside and target region where blocked off. Prominent lines are marked by letters corresponding to those transitions listed in Table I. The initial conditions are for a 20 J laser shot with a 5 Torr background pressure.

27

Fig. 7(b)-A synthetic spectrum for the rearward moving plasma. In this case the frontside and target have been blocked off.

DISTRIBUTION LIST

DEPARTMENT OF DEFENSE

ASSISTANT SECRETARY OF DEFENSE
COMM, CMD, CONT 7 INTELL
WASHINGTON, DC 20301

DIRECTOR
COMMAND CONTROL TECHNICAL CENTER
PENTAGON RM BE 685
WASHINGTON, DC 20301
  01CY ATTN C-650
  01CY ATTN C-312 R. MASON

DIRECTOR
DEFENSE ADVANCED RSCH PROJ AGENCY
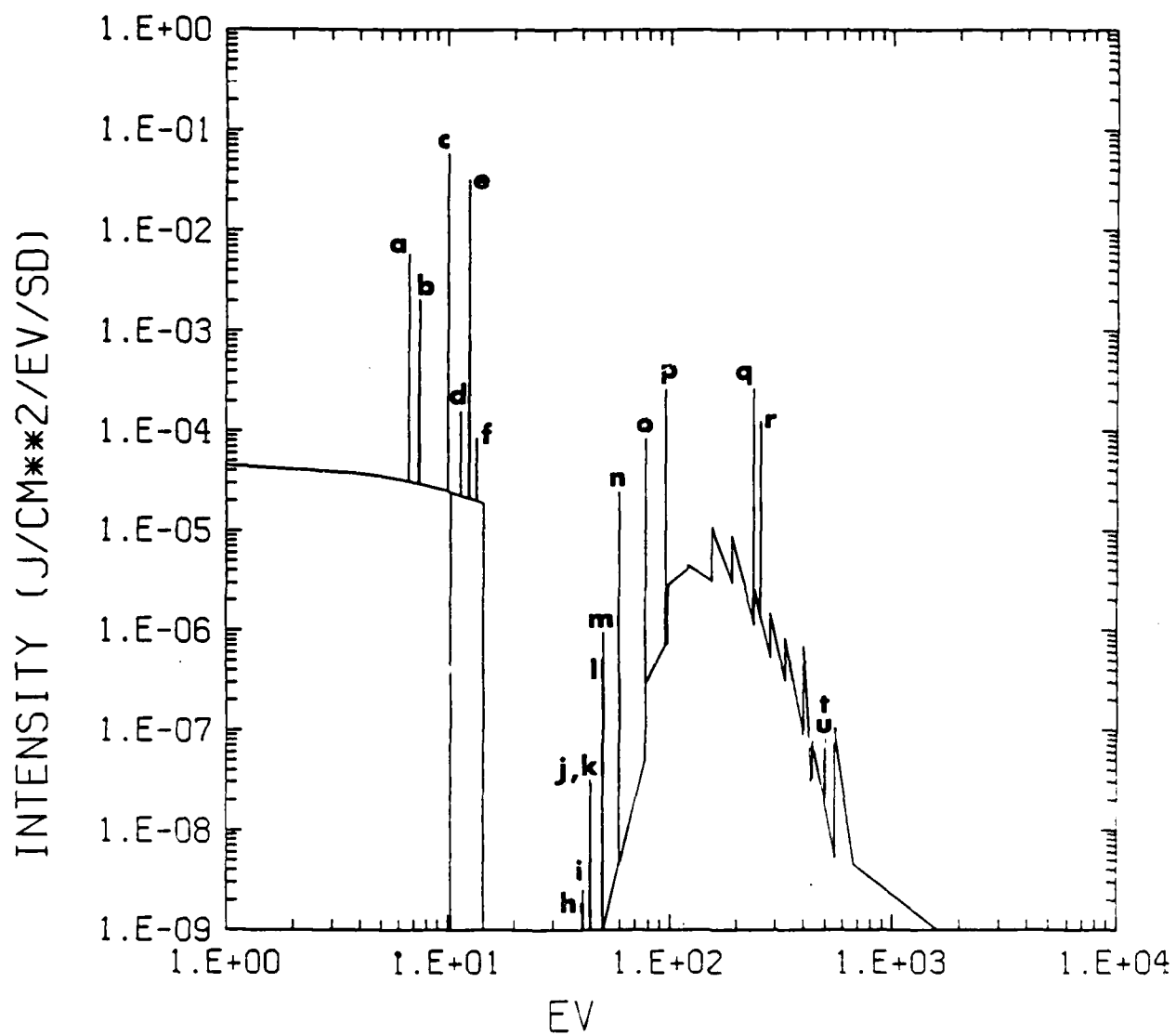ARCHITECT BUILDING
1400 WILSON BLVD.
ARLINGTON, VA 22209
  01CY ATTN NUCLEAR
      MONITORING RESEARCH
  01CY ATTN STRATEGIC TECH OFFICE

DEFENSE COMMUNICATION ENGINEER CENTER
1860 WIEHLE AVENUE
RESTON, VA 22090
  01CY ATTN CODE R410
  01CY ATTN CODE R812

DIRECTOR
DEFENSE NUCLEAR AGENCY
WASHINGTON, DC 20305
  01CY ATTN STVL
  04CY ATTN TITL
  01CY ATTN DDST
  03CY ATTN RAAE

COMMANDER
FIELD COMMAND
DEFENSE NUCLEAR AGENCY
KIRTLAND, AFB, NM 87115
  01CY ATTN FCPR

DEFENSE NUCLEAR AGENCY
SAO/DNA
BUILDING 20676
KIRTLAND AFB, NM 87115
  01CY D.C. THORNBURG

DIRECTOR
INTERSERVICE NUCLEAR WEAPONS SCHOOL
KIRTLAND AFB, NM 87115
  01CY ATTN DOCUMENT CONTROL

JOINT PROGRAM MANAGEMENT OFFICE
WASHINGTON, DC 20330
  01CY ATTN J-3 WWMCCS EVALUATION
      OFFICE

DIRECTOR
JOINT STRAT TGT PLANNING STAFF
OFFUTT AFB
OMAHA, NB 68113
  01CY ATTN JSTPS/JLKS
  01CY ATTN JPST G. GOETZ

CHIEF
LIVERMORE DIVISION FLD COMMAND DNA
DEPARTMENT OF DEFENSE
LAWRENCE LIVERMORE LABORATORY
P.O. BOX 808
LIVERMORE, CA 94550
  01CY ATTN FCPRL

COMMANDANT
NATO SCHOOL (SHAPE)
APO NEW YORK 09172
  01CY ATTN U.S. DOCUMENTS OFFICER

UNDER SECY OF DEF FOR RSCH & ENGRG
DEPARTMENT OF DEFENSE
WASHINGTON, DC 20301
  01CY ATTN STRATEGIC & SPACE
      SYSTEMS (OS)

COMMANDER/DIRECTOR
ATMOSPHERIC SCIENCES LABORATORY
U.S. ARMY ELECTRONICS COMMAND
WHITE SANDS MISSILE RANGE, NM 88002
  01CY ATTN DELAS-EO, F. NILES

DIRECTOR
BMD ADVANCED TECH CTR
HUNTSVILLE OFFICE
P.O. BOX 1500
HUNTSVILLE, AL 35807
  01CY ATTN ATC-T MELVIN T. CAPPS
  01CY ATTN ATC-O W. DAVIES
  01CY ATTN ATC-R DON RUSS

PROGRAM MANAGER
BMD PROGRAM OFFICE
5001 EISENHOWER AVENUE
ALEXANDRIA, VA 22333
  01CY   ATTN DACS-BMT   J. SHEA

COMMANDER
U.S. ARMY COMM-ELEC ENGRG INSTAL AGY
FT. HUACHUCA, AZ 85613
  01CY   ATTN CCC-EMEO   GEORGE LANE

COMMANDER
U.S. ARMY FOREIGN SCIENCE & TECH CTR
220 7TH STREET, NE
CHARLOTTESVILLE, VA 22901
  01CY   ATTN DRXST-SD

COMMANDER
U.S. ARMY MATERIAL DEV & READINESS CMD
5001 EISENHOWER AVENUE
ALEXANDRIA, VA 22333
  01CY   ATTN DRCLDC   J.A. BENDER

COMMANDER
U.S. ARMY NUCLEAR AND CHEMICAL AGENCY
7500 BACKLICK ROAD
BLDG 2073
SPRINGFIELD, VA 22150
  01CY   ATTN LIBRARY

DIRECTOR
U.S. ARMY BALLISTIC RESEARCH
LABORATORY
ABERDEEN PROVING GROUND, MD 21005
  01CY   ATTN TECH LIBRARY,
         EDWARD BAICY

COMMANDER
U.S. ARMY SATCOM AGENCY
FT. MONMOUTH, NJ 07703
  01CY   ATTN DOCUMENT CONTROL

COMMANDER
U.S. ARMY MISSILE INTELLIGENCE AGENCY
REDSTONE ARSENAL, AL 35809
  01CY   ATTN JIM GAMBLE

DIRECTOR
U.S. ARMY TRADOC SYSTEMS ANALYSIS
ACTIVITY
WHITE SANDS MISSILE RANGE, NM 88002
  01CY   ATTN ATAA-SA
  01CY   ATTN TCC/F. PAYAN JR.
  01CY   ATTN ATTA-TAC   LTC J. HESSE

COMMANDER
NAVAL ELECTRONIC SYSTEMS COMMAND
WASHINGTON, DC 20360
  01CY   ATTN NAVALEX 034   T. HUGHES
  01CY   ATTN PME 117
  01CY   ATTN PME 117-T
  01CY   ATTN CODE 5011

COMMANDING OFFICER
NAVAL INTELLIGENCE SUPPORT CTR
4301   SUITLAND ROAD, BLDG. 5
WASHINGTON, DC 20390
  01CY   ATTN MR. DUBBIN   STIC 12
  01CY   ATTN NISC-50
  01CY   ATTN CODE 5404   J. GALET

COMMANDER
NAVAL OCEAN SYSTEMS CENTER
SAN DIEGO, CA 92152
  01CY   ATTN J. FERGUSON

NAVAL RESEARCH LABORATORY
WASHINGTON, DC 20375
  01CY   ATTN CODE 4700   S.L. Ossakow
         26 CYS IF UNCLASS
         (01CY IF CLASS)
         ATTN CODE 4780   J.D. HUBA, 5
         CYS IF UNCLASS, 01CY IF CLA
  01CY   ATTN CODE 4701   I. VITKOVITS
  01CY   ATTN CODE 7500
  01CY   ATTN CODE 7550
  01CY   ATTN CODE 7580
  01CY   ATTN CODE 7551
  01CY   ATTN CODE 7555
  01CY   ATTN CODE 4730   E. MCLEAN
  01CY   ATTN CODE 4752
  01CY   ATTN CODE 4730   B. RIPIN
  20CY   ATTN CODE 2628
  01CY   ATTN CODE 1004 (P. MANGE)
  02CY   ATTN CODE 8344 (M. KAPLAN)

COMMANDER
NAVAL SPACE SURVEILLANCE SYSTEM
DAHLGREN, VA 22448
  01CY   ATTN CAPT J.H. BURTON

OFFICER-IN-CHARGE
NAVAL SURFACE WEAPONS CENTER
WHITE OAK, SILVER SPRING, MD 20910
  01CY   ATTN CODE F31

DIRECTOR
STRATEGIC SYSTEMS PROJECT OFFICE
DEPARTMENT OF THE NAVY
WASHINGTON, DC 20376
  01CY ATTN NSP-2141
  01CY ATTN NSSP-2722 FRED WIMBERLY

COMMANDER
NAVAL SURFACE WEAPONS CENTER
DAHLGREN LABORATORY
DAHLGREN, VA 22448
  01CY ATTN CODE DF-14 R. BUTLER

OFFICER OF NAVAL RESEARCH
ARLINGTON, VA 22217
  01CY ATTN CODE 465
  01CY ATTN CODE 461
  01CY ATTN CODE 402
  01CY ATTN CODE 420
  01CY ATTN CODE 421

COMMANDER
AEROSPACE DEFENSE COMMAND/XPD
DEPARTMENT OF THE AIR FORCE
ENT AFB, CO 80912
  01CY ATTN XPDQQ
  01CY ATTN XP

AIR FORCE GEOPHYSICS LABORATORY
HANSCOM AFB, MA 01731
  01CY ATTN OPR HAROLD GARDNER
  01CY ATTN LKB
      KENNETH S.W. CHAMPION
  01CY ATTN OPR ALVA T. STAIR
  01CY ATTN PHD JURGEN BUCHAU
  01CY ATTN PHD JOHN P. MULLEN

AF WEAPONS LABORATORY
KIRTLAND AFT, NM 87117
  01CY ATTN SUL
  01CY ATTN CA ARTHUR H. GUENTHER

AFTAC
PATRICK AFB, FL 32925
  01CY ATTN TN

WRIGHT AERONAUTICAL LABORATORIES
WRIGHT-PATTERSON AFB, OH 45433-6543
  01CY ATTN AAAI WADE HUNT
  01CY ATTN AAAI ALLEN JOHNSON

DEPUTY CHIEF OF STAFF
RESEARCH, DEVELOPMENT, & ACQ
DEPARTMENT OF THE AIR FORCE
WASHINGTON, DC 20330
  01CY ATTN AFRDQ

HEADQUARTERS
ELECTRONIC SYSTEMS DIVISION
DEPARTMENT OF THE AIR FORCE
HANSCOM AFB, MA 01731-5000
  01CY ATTN J. DEAS
      ESD/SCD-4

COMMANDER
FOREIGN TECHNOLOGY DIVISION, AFSC
WRIGHT-PATTERSON AFB, OH 45433
  01CY ATTN NICD LIBRARY
  01CY ATTN ETDP B. BALLARD

COMMANDER
ROME AIR DEVELOPMENT CENTER, AFSC
GRIFFISS AFB, NY 13441
  01CY ATTN DOC LIBRARY/TSLD
  01CY ATTN OCSE V. COYNE

STRATEGIC AIR COMMAND/XPFS
OFFUTT AFB, NB 68113
  01CY ATTN XPFS

SAMSO/MN
NORTON AFB, CA 92409
(MINUTEMAN)
  01CY ATTN MNNL

COMMANDER
ROME AIR DEVELOPMENT CENTER, AFSC
HANSCOM AFB, MA 01731
  01CY ATTN EEP A. LORENTZEN

DEPARTMENT OF ENERGY
LIBRARY ROOM G-042
WASHINGTON, DC 20545
  01CY ATTN DOC CON FOR A. LABOWITZ

DEPARTMENT OF ENERGY
ALBUQUERQUE OPERATIONS OFFICE
P.O. BOX 5400
ALBUQUERQUE, NM 87115
  01CY ATTN DOC CON FOR D. SHERWOOD

EG&G, INC.
LOS ALAMOS DIVISION
P.O. BOX 809
LOS ALAMOS, NM 85544
  01CY   ATTN DOC CON FOR J. BREEDLOVE

UNIVERSITY OF CALIFORNIA
LAWRENCE LIVERMORE LABORATORY
P.O. BOX 808
LIVERMORE, CA 94550
  01CY   ATTN DOC CON FOR TECH INFO
          DEPT
  01CY   ATTN DOC CON FOR L-389 R. OTT
  01CY   ATTN DOC CON FOR L-31 R. HAGER

LOS ALAMOS NATIONAL LABORATORY
P.O. BOX 1663
LOS ALAMOS, NM 87545
  01CY   ATTN DOC CON FOR J. WOLCOTT
  01CY   ATTN DOC CON FOR R.F. TASCHEK
  01CY   ATTN DOC CON FOR E. JONES
  01CY   ATTN DOC CON FOR J. MALIK
  01CY   ATTN DOC CON FOR R. JEFFRIES
  01CY   ATTN DOC CON FOR J. ZINN
  01CY   ATTN DOC CON FOR D. WESTERVELT
  01CY   ATTN D. SAPPENFIELD

LOS ALAMOS NATIONAL LABORATORY
MS D438
LOS ALAMOS, NM 87545
  01CY   ATTN S.P. GARY
  01CY   ATTN J. BOROVSKY

SANDIA LABORATORIES
P.O. BOX 5800
ALBUQUERQUE, NM 87115
  01CY   ATTN DOC CON FOR W. BROWN
  01CY   ATTN DOC CON FOR A.
          THORNBROUGH
  01CY   ATTN DOC CON FOR T. WRIGHT
  01CY   ATTN DOC CON FOR D. DAHLGREN
  01CY   ATTN DOC CON FOR 3141
  01CY   ATTN DOC CON FOR SPACE PROJECT
          DIV

SANDIA LABORATORIES
LIVERMORE LABORATORY
P.O. BOX 969
LIVERMORE, CA 94550
  01CY   ATTN DOC CON FOR B. MURPHEY
  01CY   ATTN DOC CON FOR T. COOK

OFFICE OF MILITARY APPLICATION
DEPARTMENT OF ENERGY
WASHINGTON, DC 20545
  01CY   ATTN DOC CON DR. YO SONG

NATIONAL OCEANIC & ATMOSPHERIC ADMIN
ENVIRONMENTAL RESEARCH LABORATORIES
DEPARTMENT OF COMMERCE
BOULDER, CO 80302
  01CY   ATTN R. GRUBB

DEPARTMENT OF DEFENSE CONTRACTORS

AEROSPACE CORPORATION
P.O. BOX 92957
LOS ANGELES, CA 90009
  01CY   ATTN I. GARFUNKEL
  01CY   ATTN T. SALMI
  01CY   ATTN V. JOSEPHSON
  01CY   ATTN S. BOWER
  01CY   ATTN D. OLSEN

ANALYTICAL SYSTEMS ENGINEERING CORP
5 OLD CONCORD ROAD
BURLINGTON, MA 01803
  01CY   ATTN RADIO SCIENCES

AUSTIN RESEARCH ASSOC., INC.
1901 RUTLAND DRIVE
AUSTIN, TX 78758
  01CY   ATTN L. SLOAN
  01CY   ATTN R. THOMPSON

BERKELEY RESEARCH ASSOCIATES, INC.
P.O. BOX 983
BERKELEY, CA 94701
  01CY   ATTN J. WORKMAN
  01CY   ATTN C. PRETTIE
  01CY   ATTN S. BRECHT

BOEING COMPANY, THE
P.O. BOX 3707
SEATTLE, WA 98124
  01CY   ATTN G. KEISTER
  01CY   ATTN D. MURRAY
  01CY   ATTN G. HALL
  01CY   ATTN J. KENNEY

CHARLES STARK DRAPER LABORATORY, INC
555 TECHNOLOGY SQUARE
CAMBRIDGE, MA 02139
  01CY   ATTN D.B. COX
  01CY   ATTN J.P. GILMORE

COMSAT LABORATORIES
22300 COMSAT DRIVE
CLARKSBURG, MD 20871
  01CY ATTN G. HYDE

CORNELL UNIVERSITY
DEPARTMENT OF ELECTRICAL ENGINEERING
ITHACA, NY 14850
  01CY ATTN D.T. FARLEY, JR.

ELECTROSPACE SYSTEMS, INC.
BOX 1359
RICHARDSON, TX 75080
  01CY ATTN H. LOGSTON
  01CY ATTN SECURITY (PAUL PHILLIPS)

EOS TECHNOLOGIES, INC.
606 Wilshire Blvd.
Santa Monica, CA 90401
  01CY ATTN C.B. GABBARD
  01CY ATTN R. LELEVIER

GEOPHYSICAL INSTITUTE
UNIVERSITY OF ALASKA
FAIRBANKS, AK 99701
  (ALL CLASS ATTN: SECURITY OFFICER)
  01CY ATTN T.N. DAVIS (UNCLASS ONLY)
  01CY ATTN NEAL BROWN (UNCLASS ONLY)

GTE SYLVANIA, INC.
ELECTRONICS SYSTEMS GRP-EASTERN DIV
77 A STREET
NEEDHAM, MA 02194
  01CY ATTN DICK STEINHOF

HSS, INC.
2 ALFRED CIRCLE
BEDFORD, MA 01730
  01CY ATTN DONALD HANSEN

ILLINOIS, UNIVERSITY OF
107 COBLE HALL
150 DAVENPORT HOUSE
CHAMPAIGN, IL 61820
  (ALL CORRES ATTN DAN MCCLELLAND)
  01CY ATTN K. YEH

INSTITUTE FOR DEFENSE ANALYSES
1801 NO. BEAUREGARD STREET
ALEXANDRIA, VA 22311
  01CY ATTN J.M. AEIN
  01CY ATTN ERNEST BAUER
  01CY ATTN HANS WOLFARD
  01CY ATTN JOEL BENGSTON

INTL TEL & TELEGRAPH CORPORATION
500 WASHINGTON AVENUE
NUTLEY, NJ 07110
  01CY ATTN TECHNICAL LIBRARY

JAYCOR
11011 TORREYANA ROAD
P:O: BOX 85154
SAN DIEGO, CA 92138
  01CY ATTN J.L: SPERLING

JOHNS HOPKINS UNIVERSITY
APPLIED PHYSICS LABORATORY
JOHNS HOPKINS ROAD
LAUREL, MD 20810
  01CY ATTN DOCUMENT LIBRARIAN
  01CY ATTN THOMAS POTEMRA
  01CY ATTN JOHN DASSOULAS

KAMAN SCIENCES CORP
P.O. BOX 7463
COLORADO SPRINGS, CO 80933
  01CY ATTN T. MEAGHER

KAMAN TEMPO-CENTER FOR ADVANCED
STUDIES
816 STATE STREET (P.O DRAWER QQ)
SANTA BARBARA, CA 93102
  01CY ATTN DASIAC
  01CY ATTN WARREN S. KNAPP
  01CY ATTN WILLIAM MCNAMARA
  01CY ATTN B. GAMBILL

LINKABIT CORP
10453 ROSELLE
SAN DIEGO, CA 92121
  01CY ATTN IRWIN JACOBS

LOCKHEED MISSILES & SPACE CO., INC
P.O. BOX 504
SUNNYVALE, CA 94088
  01CY ATTN DEPT 60-12
  01CY ATTN D.R. CHURCHILL

LOCKHEED MISSILES & SPACE CO., INC.
3251 HANOVER STREET
PALO ALTO, CA 94304
  01CY ATTN MARTIN WALT DEPT 52-12
  01CY ATTN W.L. IMHOF DEPT 52-12
  01CY ATTN RICHARD G. JOHNSON
       DEPT 52-12
  01CY ATTN J.B. CLADIS DEPT 52-12

MARTIN MARIETTA CORP
ORLANDO DIVISION
P.O. BOX 5837
ORLANDO, FL 32805
  01CY ATTN R. HEFFNER

MCDONNEL DOUGLAS CORPORATION
5301 BOLSA AVENUE
HUNTINGTON BEACH, CA 92647
  01CY ATTN N. HARRIS
  01CY ATTN J. MOULE
  01CY ATTN GEORGE MROZ
  01CY ATTN W. OLSON
  01CY ATTN R.W. HALPRIN
  01CY ATTN TECHNICAL
       LIBRARY SERVICES

MISSION RESEARCH CORPORATION
735 STATE STREET
SANTA BARBARA, CA 93101
  01CY ATTN P. FISCHER
  01CY ATTN W.F. CREVIER
  01CY ATTN STEVEN L. GUTSCHE
  01CY ATTN R. BOGUSCH
  01CY ATTN R. HENDRICK
  01CY ATTN RALPH KILB
  01CY ATTN DAVE SOWLE
  01CY ATTN F. FAJEN
  01CY ATTN M. SCHEIBE
  01CY ATTN CONRAD L. LONGMIRE
  01CY ATTN B. WHITE
  01CY ATTN R. STAGAT
  01CY ATTN D. KNEPP
  01CY ATTN C. RINO

MISSION RESEARCH CORP.
1720 RANDOLPH ROAD, S.E.
ALBUQUERQUE, NM 87106
  01CY R. STELLINGWERF
  01CY M. ALME
  01CY L. WRIGHT

MITRE CORP
WESTGATE RESEARCH PARK
1820 DOLLY MADISON BLVD
MCLEAN, VA 22101
  01CY ATTN W. HALL
  01CY ATTN W. FOSTER

PACIFIC-SIERRA RESEARCH CORP
12340 SANTA MONICA BLVD.
LOS ANGELES, CA 90025
  01CY ATTN E.C. FIELD, JR.

PENNSYLVANIA STATE UNIVERSITY
IONOSPHERE RESEARCH LAB
318 ELECTRICAL ENGINEERING EAST
UNIVERSITY PARK, PA 16802
  (NO CLASS TO THIS ADDRESS)
  01CY ATTN IONOSPHERIC RESEARCH L/

PHOTOMETRICS, INC.
4 ARROW DRIVE
WOBURN, MA 01801
  01CY ATTN IRVING L. KOFSKY

PHYSICAL DYNAMICS, INC.
P.O. BOX 3027
BELLEVUE, WA 98009
  01CY ATTN E.J. FREMOUW

PHYSICAL DYNAMICS, INC.
P.O. BOX 10367
OAKLAND, CA 94610
  ATTN A. THOMSON

R & D ASSOCIATES
P.O. BOX 9695
MARINA DEL REY, CA 90291
  01CY ATTN FORREST GILMORE
  01CY ATTN WILLIAM B. WRIGHT, JR.
  01CY ATTN WILLIAM J. KARZAS
  01CY ATTN H. ORY
  01CY ATTN C. MACDONALD
  01CY ATTN BRIAN LAMB
  01CY ATTN MORGAN GROVER

RAYTHEON CO.
528 BOSTON POST ROAD
SUDBURY, MA 01776
  01CY ATTN BARBARA ADAMS

RIVERSIDE RESEARCH INSTITUTE
330 WEST 42nd STREET
NEW YORK, NY 10036
  01CY ATTN VINCE TRAPANI

SCIENCE APPLICATIONS
  INTERNATIONAL INCORPORATED
1150 PROSPECT PLAZA
LA JOLLA, CA 92037
  01CY ATTN LEWIS M. LINSON
  01CY ATTN DANIEL A. HAMLIN
  01CY ATTN E. FRIEMAN
  01CY ATTN E.A. STRAKER
  01CY ATTN CURTIS A. SMITH

SCIENCE APPLICATIONS
  INTERNATIONAL CORPORATION
1710 GOODRIDGE DR.
MCLEAN, VA 22102
  01CY J. COCKAYNE
  01CY E. HYMAN

SRI INTERNATIONAL
333 RAVENSWOOD AVENUE
MENLO PARK, CA 94025
  01CY ATTN J. CASPER
  01CY ATTN DONALD NEILSON
  01CY ATTN ALAN BURNS
  01CY ATTN G. SMITH
  01CY ATTN R. TSUNODA
  01CY ATTN DAVID A. JOHNSON
  01CY ATTN WALTER G. CHESNUT
  01CY ATTN CHARLES L. RINO
  01CY ATTN WALTER JAYE
  01CY ATTN J. VICKREY
  01CY ATTN RAY L. LEADABRAND
  01CY ATTN G. CARPENTER
  01CY ATTN G. PRICE
  01CY ATTN R. LIVINGSTON
  01CY ATTN V. GONZALES
  01CY ATTN D. MCDANIEL

TECHNOLOGY INTERNATIONAL CORP
75 WIGGINS AVENUE
BEDFORD, MA 01730
  01CY ATTN W.P. BOQUIST

TRW DEFENSE & SPACE SYS GROUP
ONE SPACE PARK
REDONDO BEACH, CA 90278
  01CY ATTN R. K. PLEBUCH
  01CY ATTN S. ALTSCHULER
  01CY ATTN D. DEE
  01CY ATTN D/ STOCKWELL
      SNTF/1575

VISIDYNE
SOUTH BEDFORD STREET
BURLINGTON, MA 01803
  01CY ATTN W. REIDY
  01CY ATTN J. CARPENTER
  01CY ATTN C. HUMPHREY

UNIVERSITY OF PITTSBURGH
PITTSBURGH, PA 15213
  01CY ATTN: N. ZABUSKY

DIRECTOR OF RESEARCH
U.S. NAVAL ACADEMY
ANNAPOLIS, MD 21402
            2 COPIES

Code 2628   22 copies

Code 1220   1 copy

Records   1 copy